Electronic Supplementary Information for

Continuous-flow hydroprocessing of long-chain fatty acids: reaction pathways and the impact of lignin-derived aromatics towards efficient deoxygenation

Rita Assis dos Santos,*[ab] Arij Ben Hassine,[b] Pedro José Sanches Filho,[b] M. Joana Neiva Correia,[ac] and Pedro S. F. Mendes*[ab]

[a]Departamento de Engenharia Química, Instituto Superior Técnico, Universidade de Lisboa, Av. Rovisco Pais, 1049-001 Lisboa, Portugal

[b]Centro de Química Estrutural, Institute of Molecular Sciences, Instituto Superior Técnico, Universidade de Lisboa, Av. Rovisco Pais, 1049-001 Lisboa, Portugal

[c]Centro de Recursos Naturais e Ambiente, Instituto Superior Técnico, Universidade de Lisboa, Av. Rovisco Pais, 1049-001 Lisboa, Portugal

*Corresponding authors: rita.assis.santos@tecnico.ulisboa.pt (Rita Assis dos Santos), pedro.f.mendes@tecnico.ulisboa.pt (Pedro S. F. Mendes)

Table of contents

1. Experimental section

This chapter includes both the materials and the methodology used in this work. It begins by describing and characterising the materials, namely the feedstocks and the catalyst. This is followed by a brief description of the experimental setup used for the catalytic tests. Subsequently, the analytical methods utilised for the characterisation and quantification of gaseous and liquid products are presented. Finally, a dedicated section outlines the analytical data treatment applied to enable the interpretation and analysis of the results obtained.

1.1. Feedstocks

For the catalytic essays, oleic acid from *Fischer Scientific* (A16663.0J, lots 2345928 and 2408090) and guaiacol from *Sigma-Aldrich* (W253200, lot SHBS1735) were purchased and characterised by Gas Chromatography (GC) equipped with a Flame Ionisation Detector (FID) (refer to Section 1.4). Guaiacol was confirmed to have a purity above 99 wt. %. Oleic acid feed composition included linoleic acid (~ 10 wt. %), palmitic acid (~ 6 wt. %) and stearic acid (~ 2 wt. %). For the co-processing essays, a mixture of oleic acid and guaiacol at a nominal 75/25 molar ratio was used. Gas chromatograms of the two feedstocks are presented in Fig. S1.

Given the high purity of guaiacol (> 99 wt. %), it was treated as a single-component feedstock. In contrast, oleic acid, while being the major compound, contained minor amounts of other fatty acids. Linoleic acid (C_{18}:2) and stearic acid (C_{18}:0) share the same carbon chain length as oleic acid (C_{18}:1) and readily interconvert via hydrogenation reactions. As such, these species were considered part of the oleic acid reaction network and do not interfere with the reaction pathway analysis. Palmitic acid (C_{16}:0), however, has a shorter carbon chain and can generate deoxygenation products overlapping with those derived from oleic acid (e.g., C_{16} from palmitic acid hydrodeoxygenation (HDO) or from heptadecane hydrogenolysis). Despite its minor concentration, its contribution was assessed through the stoichiometric analysis presented in Section 2.2 to validate the reaction pathways.

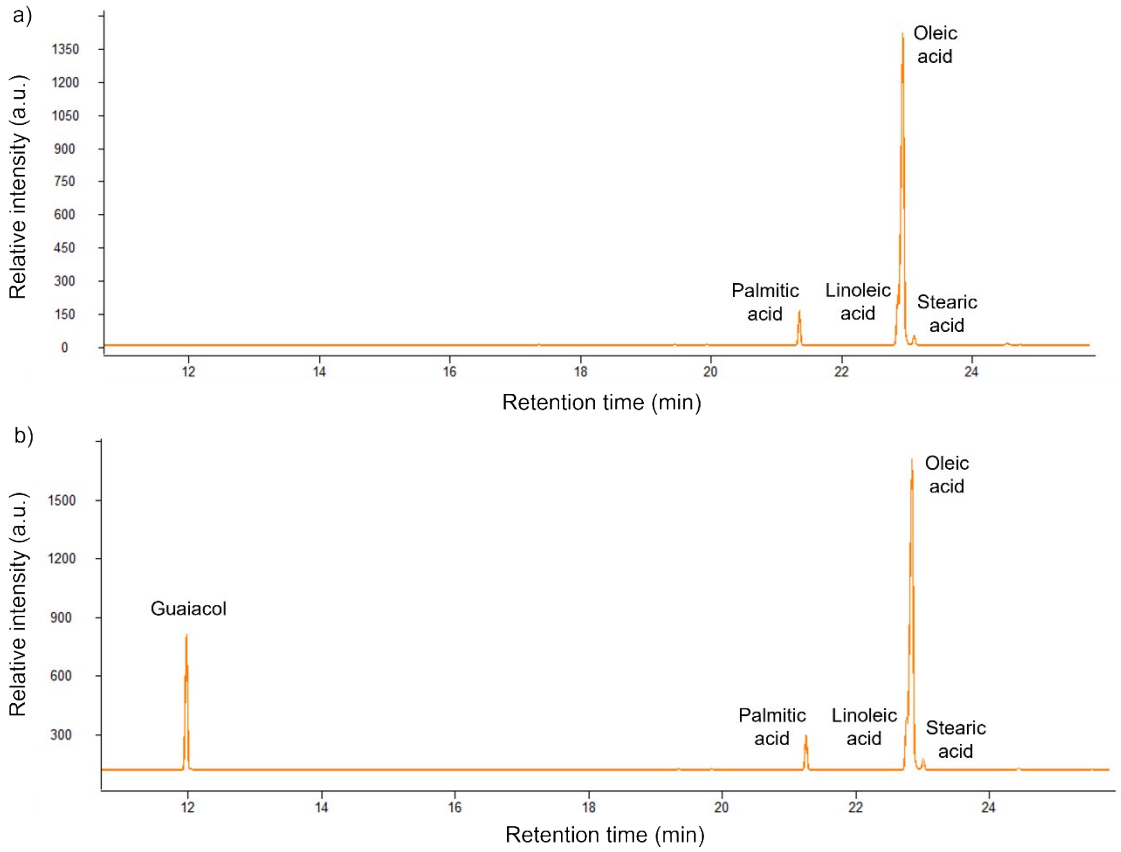

Fig. S1 Snippet of gas chromatograms for the feedstocks used: a) oleic acid, b) oleic acid/guaiacol mixture (75/25 molar ratio).

1.2. Catalyst preparation and characterisation

Nickel was chosen as the metal function, offering a good balance between deoxygenation efficiency and economic feasibility compared to noble metals [1,2]. ZSM-5 zeolite was selected for its strong Brønsted acidity, with the aim of promoting HDO over decarbonylation (DCO) and decarboxylation (DCO_x) [3]. Furthermore, the choice of a well-known representative Ni/ZSM-5 allowed to establish reliable reaction pathways and, consequently, evaluate mixture effects.

For the catalyst preparation, NH_4ZSM-5 CBV8014 (Si/Al = 40) from *Zeolyst* and nickel supported on silica-alumina (65Ni/SiO_2-Al_2O_3, 208779) from *Sigma-Aldrich* were used. NH_4ZSM-5 and 65Ni/SiO_2-Al_2O_3 were calcined at 450 ºC in an air flow of 4 L/h/$g_{catalyst}$, over 6 h and 3 h, respectively. A plateau at 200 ºC for 1 h was included and the heating rate between plateaus was 2 ºC/min. After calcination, these were stored for 48 h in a closed chamber containing an oversaturated sodium carbonate solution, maintaining relative humidity above 80 %. The two catalysts were then mechanically mixed using a mortar and pestle for 30 min in adequate proportions to obtain a target nickel concentration of 20 wt. % (20Ni/HZSM-5). Then, the mixed catalyst was calcined again under air at 550 ºC for 5 h. All the remaining calcination conditions remained unchanged from the ones previously described. The catalyst powder was pressed into 0.063 – 0.125 mm pellets under 1.5 ton pressure for 30 s. The catalyst was reduced *ex-situ* with a H_2 flow of 4 L/h/$g_{catalyst}$ to a reduction temperature of 450 ºC for 2 h. Before H_2 pre-treatment,

the reactor was purged with N_2 with a flow five times the reactor volume. A temperature plateau at 150 ºC for 1 h was included, and the heating rate between plateaus was 10 ºC/min. For catalytic essays, the catalyst used was always saturated for at least 24 h prior to use.

The selected zeolite has been characterised in the literature, and its textural properties are summarised in Table S1. These properties were obtained by N_2 physisorption, where the micropore volume was determined using the t-plot method, while the mesopore size distribution was determined by applying the Barrett-Joyner-Halenda method [4].

Table S1 HZM-5 textural properties [4].

Material	**Volume (cm^3/g)**		
	Micro	**Meso**	**Total**
HZSM-5	0.16	0.08	0.24

From Table S1, it is evident that micropores are the major contributors to the total pore volume, which is consistent with the zeolite's MFI framework (three-dimensional network with 10-membered ring channels, pore diameter of 5.1 - 5.6 Å) [5].

Additionally, Table S2 presents the amount of Lewis and Brønsted acid sites, determined by Fourier transform infrared spectroscopy of adsorbed pyridine [4].

Table S2 HZM-5 acid properties [4].

Material	**Lewis acid sites (µmol/g)**		**Brønsted acid sites (µmol/g)**	
	150 ºC	**350 ºC**	**150 ºC**	**350 ºC**
HZSM-5	37	33	336	283

Table S2 indicates that the zeolite contains a higher amount of Brønsted acid sites compared to Lewis acid sites. At 150 ºC, all acid sites are probed with pyridine, whereas at higher temperatures, such as 350 ºC, only the strong acid sites remain probed with pyridine. Thus, the amount of weak acid sites was considered as the difference between the values at 150 ºC and 350 ºC [6,7]. Therefore, it is clear that most of the acid sites, both Lewis and Brønsted, are strong acid sites.

After calcination, Thermogravimetric Analysis (TGA) was conducted on the 20Ni/HZSM-5 catalyst using a SETSYS Evolution TGA 1750 instrument. The sample (10 - 15 mg) was heated from 20 ºC to 800 ºC at 10 ºC/min under an air flow of 30 mL/min. Two cycles were recorded, the second being subtracted from the first one to correct for the effect of heating on the mass and heat flow variation. TGA allowed for the calculation of the Loss On Ignition (LOI), according to Eq. S1. To ensure the LOI values were independent of ambient conditions, TGA was performed on saturated samples. These were stored for 48 h in a closed chamber containing an oversaturated sodium carbonate solution, maintaining relative humidity above 80 %.

$$LOI\ (wt.\ \%) = \frac{m_{saturated} - m_{dry}}{m_{saturated}} \times 100 \quad , \qquad \text{(Eq. S1)}$$

where $m_{saturated}$ is the mass of saturated catalyst (g) and m_{dry} is the mass of dried catalyst (g).

The respective TGA plot is presented in Fig. S2, and the LOI was calculated to be 7.3 wt. %. The profile on Fig. S2 reveals that most weight loss occurs before 220 ºC, corresponding to water

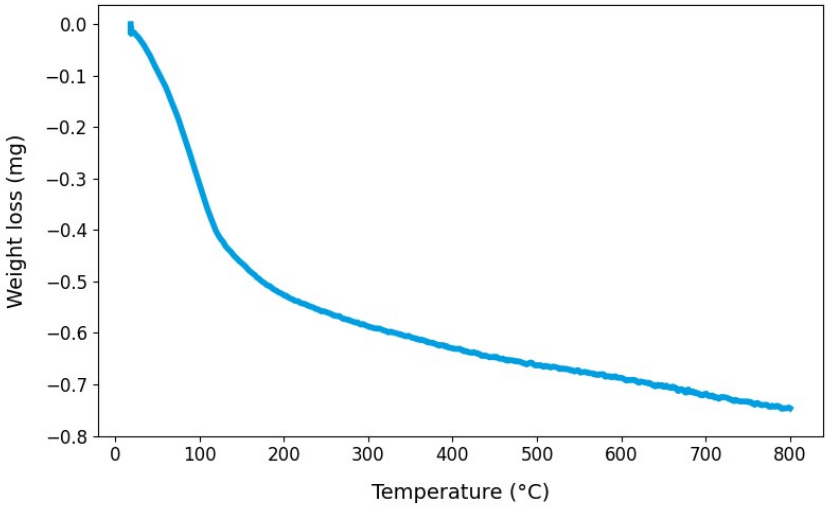

Fig. S2 20Ni/HSZM-5 TGA plot.

desorption.

The calcined 65Ni/SiO_2-Al_2O_3 and reduced 20Ni/HZSM-5 were characterised by H_2 Temperature Programmed Reduction (TPR), using an Altamira AMI-300. Around 0.1 g of calcined catalyst was loaded into the U-shaped reactor and pre-treated using argon (Ar), followed by the analysis using 30 mL/min of 5 % H_2/Ar mixture until 900 ºC with a heating ramp of 5 ºC/min. The resulting TPR profiles are presented in Fig. S3. Assuming the same nickel species were present in both samples with identical reduction stoichiometry, the normalised integrated areas indicate that roughly 61 % of the nickel was reduced with the *ex-situ* pre-treatment.

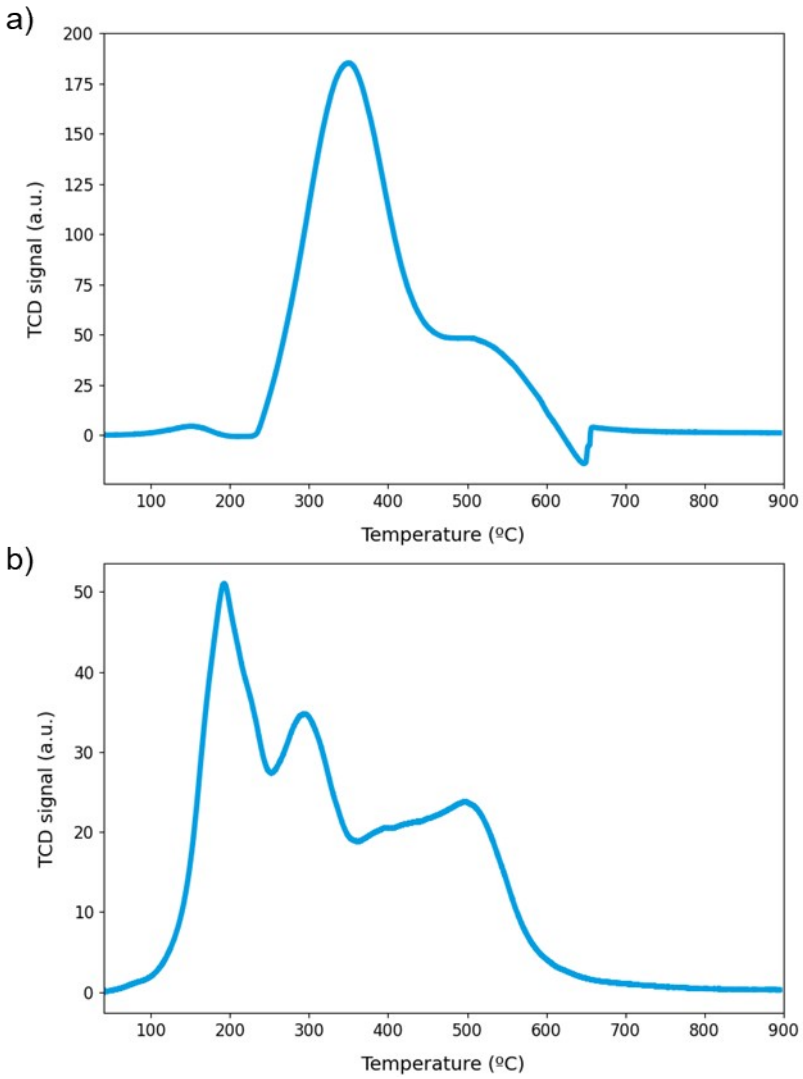

Fig. S3 H_2-TPR profiles: a) calcined 65Ni/SiO_2-Al_2O_3; b) reduced 20Ni/HZSM-5.

1.3. Experimental setup and procedure

The catalytic essays were using an automatic computerised high-throughput (HTP) unit from *PID Eng & Tech*, with a single fixed-bed reactor. Fig. S4 presents a simplified scheme of the experimental setup. The reactor is inside a hot box, a forced convection heating system, with a length of 284 mm and an internal diameter of 17.5 mm (0.3 – 1.5 g of catalyst). It is housed within a furnace that creates a 2 cm isothermal zone, where the catalyst bed is located. The H_2 flow is regulated by a mass flow controller, and the feedstock is pumped by a high-pressure metering pump, both of which are mixed inside the hot box and fed into the reactor from the bottom up (ascending flow). The feedstock vessel is pressurised and maintained under an inert N_2 atmosphere, besides being heated and equipped with a magnetic stirrer. Both the liquid feed lines and product lines are heated.

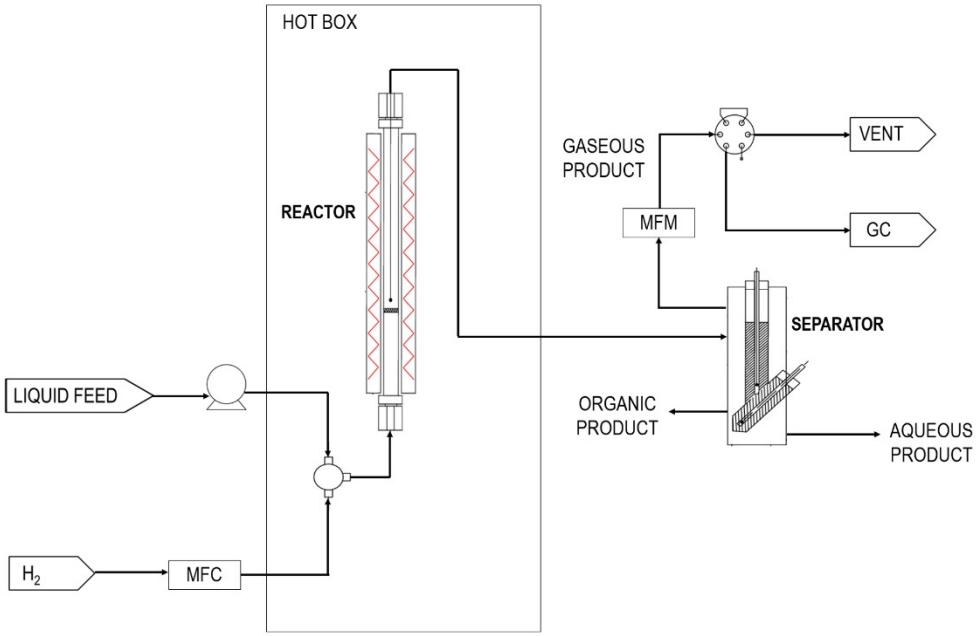

Fig. S4 Simplified experimental setup scheme. MFC = Mass Flow Controller; MFM = Mass Flow Meter.

Given that catalytic tests were conducted in a continuous reactor, maintaining a consistent particle size was essential. Heat and mass transfer limitations were estimated using standard correlations (e.g., Carberry number, Weisz-Prater criterion, Mears criterion) implemented in the *EUROKIN* gas-solid fixed-bed tool [8], and the particle diameter range was calculated to minimise diffusional limitations.

Prior to each new catalyst loading, the system was thoroughly cleaned with hexane. The catalyst bed was prepared using inert silicon carbide (SiC). Two different SiC granulometries, 1.680 mm and 1.190 mm, were used to fill the non-isothermal regions in equal heights above and below the isothermal zone. To fill the isothermal zone volume, the catalyst mass was mixed with SiC of similar granulometry (0.105 mm), with the catalyst bed dilution maintained between 10 – 90 %. To ensure the catalyst/SiC mixture remained within the isothermal zone, a thin quartz wool layer was added below and above. Leak tests with H_2 were performed to ensure system integrity at the target reaction pressure plus a 2 bar safety margin, with the test deemed successful if the pressure drop was ≤ 0.3 bar/h. Following a successful leak test, the catalyst underwent *in-situ* reduction under the same conditions described in Section 1.2. To improve operational efficiency, the reduction was carried out at the established reaction pressure, since this step followed the leak tests.

Ideally, TOS begins when the feedstock first reaches the catalyst bed. Since deoxygenation reactions involve oxygen removal, an exothermic process, a slight temperature increase would theoretically occur at that moment, even though the catalyst bed is located in an isothermal zone. However, analysis of the test data revealed that temperature variations were generally within ± 0.4 ºC after stabilisation, making it impossible to pinpoint feed introduction based on temperature

shifts. Therefore, a practical definition of TOS was applied, given the system's intricacies and dead volume. TOS was defined starting after 42 mL of feedstock had been pumped.

1.4. Product analysis

Gaseous products were continuously analysed online in real-time, whereas the liquid organic products (C_7+ fraction) underwent dilution and a derivatisation process prior to GC analysis on a separate equipment. The aqueous products, when produced, were not subject to direct analysis.

1.4.1. Gaseous products

The gaseous reaction products were analysed by the online gas chromatograph (*Agilent Technologies 8860*) coupled to the HTP unit. The system was equipped with a methanizer, a FID and two capillary columns (column #1: *Agilent Technologies HP-PLOT/Q*, 30 m x 0.530 mm x 40.0 µm; column #2: *Agilent Technologies HP-Molesieve*, 30 m x 0.530 mm x 25.0 µm). Despite this configuration, only column #1 was used for the analyses. The total analysis run time was 31 min. The program started with an oven temperature of 40 ºC held for 5 min, ramped at 10 ºC/min to 250 ºC, and was held for an additional 5 min. The inlet H_2 column flowrate was 6.8 mL/min at 7.5 psi, with a split ratio of 10:1. The FID temperature was 250 ºC, while the H_2, air and N_2 (make-up gas) flowrates were 48 mL/min, 400 mL/min and 25 mL/min, respectively.

1.4.2. Liquid products

The liquid organic products were analysed by a bidimensional gas chromatograph (*LECO Pegasus BT 4D*) coupled to a Time-Of-Flight (TOF) detector for Mass Spectrometry (MS) and equipped with an FID and an autosampler. This system includes two columns: a low-polarity *Restek Rxi-5ms GC Capillary Column* (30 m x 0.25 mm x 0.25 µm) installed in the primary oven and a mid-polarity *Restek Rxi-17Sil MS GC Capillary Column* (1.6 m x 0.25 mm x 0.25 µm) in the secondary oven, with a N_2-cooled modulator located between them. For this work, a simple one-dimensional analysis was performed, thus, the modulator was shut off. For the GC-FID, the total analysis run time was 40 min. The program started with a primary oven temperature of 40 ºC held for 3 min, ramped at 10 ºC/min to 300 ºC, and was held for an additional 11 min. The secondary oven temperature was always 5 ºC above the primary oven. The inlet H_2 column flowrate was 1.8 mL/min, with a split ratio of 10:1. The FID temperature was 300 ºC, while the H_2, air and N_2 (make-up gas) flowrates were 44 mL/min, 450 mL/min and 50 mL/min, respectively. As for the GC-TOF/MS, the acquisition rate was 100 spectra/s with a scanning range set from 40 to 900 mu. The TOF temperature was 280 ºC, the ion source temperature was set at 250 ºC, and the MS detector used electron ionisation of 70 eV. To prevent system overload due to solvent presence, the acquisition was delayed 240 s.

As mentioned previously, before any analysis, all samples underwent a derivatisation procedure (silylation, the most versatile [9,10]). The purpose of derivatisation in GC is to optimise the chromatographic properties of the compounds by improving their volatility and enhancing their detectability [9,10]. This procedure is particularly useful for compounds with functional groups that

are otherwise difficult to separate by GC, such as carboxylic acids or hydroxyl groups [9,10]. By substituting these groups, silylation typically achieves derivatives that are less polar, more volatile and exhibit increased thermal stability [9,10].

For derivatisation, approximately 0.15 - 0.25 g of each sample was weighed into a 5 mL volumetric flask and diluted to volume with dichloromethane. From this solution, 200 µL were pipetted into a 2 mL vial, 100 µL of MSTFA were added, and the final volume was adjusted to 1 mL with dichloromethane. The mixture was then heated in a sand bath for 30 min at a temperature not exceeding 80 ºC to complete derivatisation [10].

1.5. Analytical data treatment

This chapter is subdivided into two sections. First, details on the products' quantification are provided, followed by mass balance calculations.

1.5.1. Product data treatment

Product quantification was performed separately for gaseous and organic products, using GC-based analyses combined with calibration curves.

Regarding gaseous products, to determine their composition, three consecutive online gas injections were analysed for each mass balance period. After chromatogram identification, peak areas were corrected using literature-derived Response Factors (RF) and then averaged [11]. However, this literature-based approach assumes that all compounds present in the gas stream are identified, which was not the case due to the excess H_2, undetected in the installed setup. To address this, calibration curves were developed for CO, CH_4 and CO_2. For all the remaining compounds, molar fractions were corrected relative to CH_4, with H_2 assumed to account for the remainder of the gaseous stream.

As for the organic product, in contrast to the gaseous products, literature-derived RF were not used, since derivatisation alters RF relative to those of the corresponding non-derivatised compounds, thereby limiting the applicability of published data. Therefore, calibration curves were established for the main chemical families of identified compounds, namely hydrocarbons (HC), acids, esters, aldehydes, alcohols, aromatics, cyclic HC and ethers. For HC, a series of *n*-alkanes was selected, ranging from 10 carbons to 36 carbons: decane (C_{10} HC), dodecane (C_{12} HC), octadecane (C_{18} HC), hexacosane (C_{26} HC) and hexatriacontane (C_{36} HC). For acids, calibration curves were developed using decanoic acid (C_{10}:0), palmitic acid (C_{16}:0), stearic acid (C_{18}:0), oleic acid (C_{18}:1) and linoleic acid (C_{18}:2), chosen to represent both saturated and unsaturated structures across a relevant range of chain length. In the case of esters, a diverse set was utilised, including methyl palmitate (C_{17} ester), methyl oleate (C_{19} ester), decyl decanoate (C_{20} ester), methyl eicosanoate (C_{21} ester) and stearyl stearate (C_{36} ester). For aldehydes and alcohols, octadecanal (C_{18} aldehyde) and octadecanol (C_{18} alcohol) were selected, maintaining the same carbon chain length as oleic acid to ensure consistency in functional group representation. Aromatic compounds were represented by benzene for HC and guaiacol for oxygenated

aromatics, the latter being chosen considering it is one of the feedstocks used. Calibrations for cyclic compounds were performed using dodecylbenzene and dodecyl cyclohexane, selected to represent both aromatic and aliphatic cyclic structures. Additionally, the chemical family of ethers was represented by dioctadecyl ether, a symmetrical ether containing two C_{18} chains.

1.5.2. Mass balances

To validate the catalytic tests, mass balances were performed based on all products obtained: organic, aqueous and gaseous. The inlet reactant nominal flowrates (feedstock and H_2) were confirmed based on software totalizers. The organic and aqueous collection jars were weighed at the beginning and end of each mass balance, and with the mass balance time, it was possible to obtain the respective mass flowrates. When weighing was performed only at the start and end of the entire experiment, average outlet flowrates were used instead. The global mass balance followed Eq. S2.

$$F_{feed}^{in} + F_{H_2}^{in} = F_{organic}^{out} + F_{aqueous}^{out} + F_{gaseous}^{out}, \quad \text{(Eq. S2)}$$

where F_x^{in} is the inlet mass flowrates of reactants (g/h) and F_x^{out} the outlet mass flowrates of products (g/h).

Regarding gaseous products, the mass flowrate was derived from the MFM, which provides the volume of gas passed. Having the gas composition, the molar flowrates of each compound were then calculated using the ideal gas equation, based on the volumetric flowrate (MFM output). These were converted again to mass flowrates using molecular weights for each compound. This also allowed the determination of the real mass fractions.

By combining the mass flowrates of the organic, aqueous and gaseous products with the inlet flowrates, overall mass balances were closed within a relative margin of 15 % for single-feed and 18% for dual feed. In all cases, the balances were consistently negative, indicating that the outlet mass flowrate was lower than the inlet mass flowrate. This discrepancy can primarily be attributed to two factors. First, water quantification is intrinsically difficult due to evaporation losses, which may lead to an underestimation of the aqueous outlet stream. Second, the gaseous mass flowrate may also be underestimated. The gas flowrate is calculated from the outlet volumetric flowrate measured by the MFM calibrated for H_2, whereas the actual outlet stream is a multicomponent mixture. Additionally, the gas composition assumes that, aside from the identified compounds, the remainder of the stream is H_2, which may further contribute to inaccuracies in the calculated gas mass flowrate.

Additionally, feedstock conversion was calculated on a mass basis, following Eq. S3.

$$X_{feed}\,(\%) = \frac{F_{feed}^{in} - F_{organic}^{out}}{F_{feed}^{in}} \times 100, \quad \text{(Eq. S3)}$$

where X_{feed} is the conversion, F_{feed}^{in} the feedstock inlet mass flowrate (g/h) and $F_{organic}^{out}$ the feedstock outlet mass flowrate, considering exclusively the organic phase (g/h).

In cases where the outlet mass flowrate was not directly measured, it was assumed to be around 73 % of the inlet mass flowrate, based on past experience. This assumption was used exclusively for conversion calculations to ensure comparable results at iso-conversion (± 5 %).

Importantly, the stoichiometric analysis presented in Section 2.2 was performed using datasets for which outlet mass flowrates were directly measured. Therefore, the pathway interpretation relies on experimentally determined product distributions and molar relationships rather than assumed flowrate values.

The purpose of the mass balance evaluation is primarily to verify experimental consistency and ensure that the major product streams were properly accounted for. While the observed deviations introduce some uncertainty in the absolute quantification, they do not significantly affect the interpretation of reaction pathways, which are based on relative product distributions and stoichiometric relationships.

2. Oleic acid reaction pathways

This chapter provides information on oleic acid hydroprocessing pathways, as well as a stoichiometric analysis for validation. Moreover, it contains additional figures supporting the main publication.

2.1. Hydroprocessing reactions and mechanisms

The main reactions involved in oleic acid hydroprocessing are illustrated in Fig. S5. Deoxygenation proceeds primarily via three routes: HDO, DCO and DCO_x. The resulting HC can subsequently undergo other reactions such as hydrogenolysis, hydroisomerisation (HDI) or hydrocracking (HCK) [3]. The mechanisms subsequently presented, as well as the active sites primarily catalysing the reactions, are exclusively literature-based. Table S3 summarises the

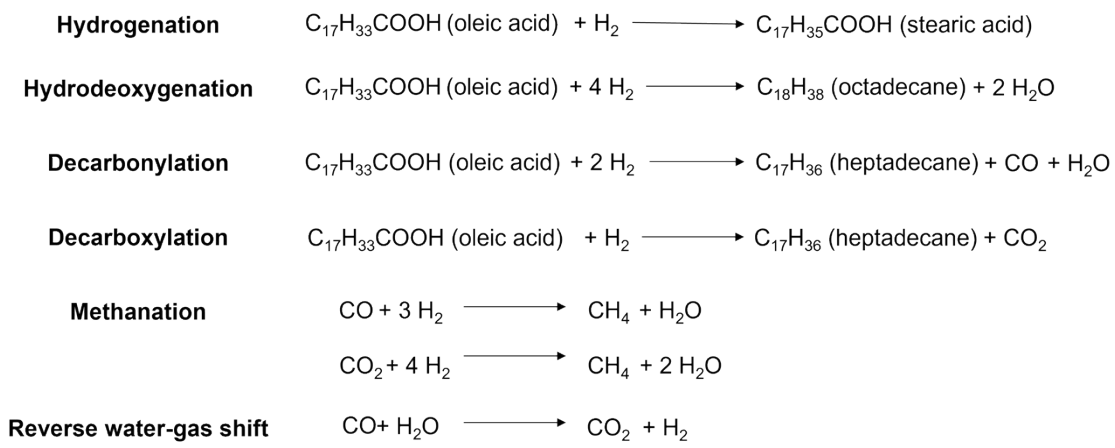

Fig. S5 Main oleic acid hydroprocessing reactions (adapted) [1,21].

mechanisms and active sites involved in hydroprocessing reactions.

Table S3 Hydroprocessing reaction mechanisms and active sites. Reaction numbering according to Fig. 1.

Reaction	Active site	Mechanism	Ref.
1 – 2 and 5 – 6 (hydrogenation)	Metal	Horiuti-Polanyi hydrogenation	[3,12–16]
3 (esterification)	Acid	Fischer esterification	[17,18]
4 (dehydration)	Acid	Intermolecular C-O and C-H bond scission	[19]
7 (hydrogenation/dehydrogenation)	Metal	Horiuti-Polanyi hydrogenation	[3,14,20]
8 (decarbonylation)	Metal	C-C bond scission (CO forming)	[1,3,18]
9 (dehydration)	Acid	C-OH bond scission	[3,18]
10 (decarboxylation)	Metal	C-C bond scission (CO_2 forming)	[3,18,21]
11 – 12 (hydroisomerisation)	Acid	Skeletal rearrangement	[1,3,22]
13 (dehydration)	Acid	-	[18]
14 (hydrogenolysis)	Metal	C-C bond scission	[3,22]

15 (hydrocracking)	Acid	β-scission	[3,22]

Hydrogenation reactions (Reactions 1 – 2, 5 – 6 and 7 in Table S3) occurring in metal sites [3,18] generally follow the Horiuti-Polanyi mechanism [12]. Molecular H_2 adsorbs onto the metal surface and dissociates into two hydrogen atoms. Unsaturated fatty acids also adsorb via their double bond, after which sequential hydrogen addition forms a half-hydrogenated intermediate and subsequently the saturated product [12,13]. The same mechanism applies to stearic acid hydrogenation to octadecanal and octadecanol, and their interconversion, where metal surface adsorption occurs via the OH group of the carboxylic function [14–16] and the molecule's functional groups [14,20], respectively.

Esterification (Reaction 3 in Table S3) proceeds on acid sites via Fischer esterification between stearic acid and octadecanol [17,18]. Overall, this reaction can be viewed as an acyl nucleophilic substitution, where the carbonyl group is first activated, facilitating nucleophilic attack by octadecanol. After the alcohol addition, the ester is formed, and a water molecule is produced [17].

Etherification (Reaction 4 in Table S3) occurs via intermolecular dehydration of octadecanol molecules on acid sites [19]. The mechanism likely involves dimer formation, where one molecule of octadecanol is adsorbed on Brønsted acid sites and interacts with another physisorbed octadecanol molecule to form a dimer. Then, the adsorbed dimer undergoes concerted C-O and C-H bond scissions to form dioctadecyl ether and water [19].

In the HDO (Reaction 9 in Table S3) pathway, the carbon chain length of the fatty acid is preserved. The reaction starts by hydrogenolysis of the C-OH bond, where the oxygen atom bonds to the active site, which donates a hydrogen atom to form an aldehyde intermediate [3]. The oxygen atom is then removed from the active site as water [3]. The aldehyde is reduced to a primary alcohol, which is subsequently dehydrated to an *n*-alkane [3].

In contrast, both DCO (Reaction 8 in Table S3) and DCO_x (Reaction 10 in Table S3) take place on metal sites and involve carbon losses as CO and CO_2, respectively. In the DCO pathway, the first step is also the reduction of the carboxyl group to the carbonyl group, similarly to HDO [1,3]. However, the oxygen from the aldehyde then proceeds to be released in the form of CO. Given the mechanistic similarities between the initial steps of HDO and DCO, selectivity between these pathways can shift if alcohol adsorption is inhibited, considering kinetics [3]. In the DCO_x route, the fatty acid adsorbs on the active sites and undergoes direct C-C bond cleavage to release CO_2 and produce the *n*-alkane shortened by one carbon [3,21].

HDI (Reactions 11 – 12 in Table S3) generally requires the cooperation of metal and acid sites [1,22]. *n*-alkanes are dehydrogenated on metal sites to *n*-alkenes [1,22]. These desorb from the metal sites and diffuse to Brønsted acid sites, where they are protonated to form reactive carbocations, which undergo skeletal rearrangements to yield isomers [1,22]. These rearrangements initially produce *i*-alkenes, which can then be hydrogenated to *i*-alkanes [22].

Depending on the position of the double bond and rearrangements, the branching occurs in different positions [22] . HCK (Reaction 15 in Table S3) proceeds on acid sites via β-scission of carbocation intermediates formed by *n*-alkene protonation [22].

In HC hydrogenolysis (Reaction 14 in Table S3), the C-C bond cleavage occurs over the reduced metal site, where the alkanes crack into CH_4 and a shorter-chain HC [3].

Under hydrogen-rich conditions, methanation and Reverse Water-Gas Shift (RWGS) reactions may occur on metal sites, making it complex to distinguish between the two types of reactions [3,21].

2.2. Stoichiometric analysis

To evaluate how the product distribution evolved with time and to gain insights into the underlying reaction pathways, a stoichiometric analysis was carried out based on molar flowrates. Stoichiometric balance calculations were based on reaction products rather than reactants, since the latter can undergo multiple reaction routes. As a starting point, only the main expected reactions, outlined in Section 2.1, of HDO, DCO and DCO_x were considered for both oleic acid and palmitic acid. Two representative samples were selected: one at TOS = 36 h and another at TOS = 60 h, for low and high TOS, respectively, to account for changes over time.

Fig. S6 summarises the workflow followed in the stoichiometric analysis. It begins with the feedstock conversion to ensure the unconverted fatty acids are not included in subsequent reaction steps. Next, both HDO and DCO are evaluated, given that water is a common product of these pathways (vide Fig. S5). This is followed by the assessment of DCO_x and RWGS reaction their relative qualitative contribution to C_{17} HC production. Methanation, hydrogenolysis and HCK reactions are evaluated last, since they are at the far end of the proposed reaction pathways, and

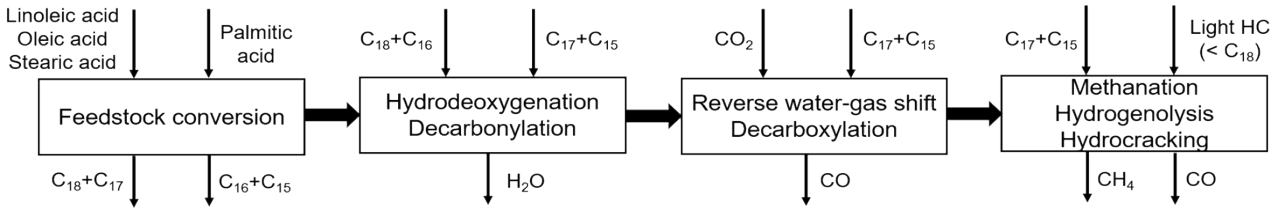

Fig. S6 Summary of the stoichiometric analysis workflow.

to evaluate the sources of CH_4 over time.

Table S4 presents the main results of the stoichiometric analysis in terms of both molar flowrates and molar percentages. The molar flowrates represent the theoretical maximum contribution in each stage, while the molar percentages facilitate comparison between theoretical and experimental values and help identify deviations.

Table S4 Summary of the stoichiometric analysis. Oleic acid includes contributions from linoleic acid and stearic acid. Positive delta values indicate excess and negative values indicate deficit compared to the experimental values.

Reaction	Product	Stoichiometry	Maximum flowrate accounted (mmol/h)		Delta (mol. %)	
			TOS = 36 h	TOS = 60 h	TOS = 36 h	TOS = 60 h
Oleic acid (OA) → C_{18} + C_{17} (global conversion)	C_{18} + C_{17}	1:1 (OA:C_{18}+C_{17})	8.8	8.3	- 44	- 47
Palmitic acid (PA) → C_{16} + C_{15} (global conversion)	C_{16} + C_{15}	1:1 (PA:C_{16}+C_{15})	0.56	0.51	+ 8.4	+ 5.2
OA/PA + 4 H_2 → C_{18}/C_{16} + 2 H_2O (HDO)	H_2O	1:2 (C_{18}/C_{16}:H_2O)	2.8	2.6	- 6.3	- 19
OA/PA + 2 H_2 → C_{17}/C_{15} + CO + H_2O (DCO)		1:1 (C_{17}/C_{15}:H_2O)	4.5	3.7		
	CO	1:1 (C_{17}/C_{15}:CO_2)	4.5 (CO)	3.7 (CO)	+ 7.5 (CO)	- 11 (CO)
CO + 3 H_2 → CH_4 + H_2O (methanation)	CH_4	1:1 (CO:CH_4)				
C_i + H_2 → C_{i-1} + CH_4 (hydrogenolysis)		1:1 (C_{i-1}:CH_4)	5.1	4.1	+ 39	+ 254
OA/PA + H_2 → C_{17}/C_{15} + CO_2 (DCO_x)	CO_2	1:1 (C_{17}/C_{15}:CO_2)	4.1 (CO)	3.3 (CO)	- 1.9 (CO)	- 39 (CO)
CO_2 + H_2 → CO + H_2O (RWGS reaction)	CO	1:1 (CO_2:CO)				

Due to inherent experimental uncertainties associated with water quantification and multicomponent gas flowrate measurements, as outlined in Section 1.5.2, the results presented should be considered interpretative. They provide stoichiometric evidence supporting the proposed reaction network to explain the observed product distribution under the studied operating conditions and are subject to the assumptions and associated experimental uncertainties described in this ESI.

2.2.1. Feedstock conversion

Based on the feedstock composition, the theoretical maximum production of C_{18} + C_{17} HC was estimated assuming complete conversion of linoleic acid, oleic acid and stearic acid. The difference between this theoretical value and the amount of oleic acid and stearic acid still present in the organic product allowed calculating the maximum yield of C_{18} + C_{17} HC. When compared to the experimentally identified HC, the observed amounts of C_{18} + C_{17} HC were lower, suggesting these compounds underwent subsequent reactions. The differences were around - 40 mol. % in both cases. The same reasoning was applied to palmitic acid, present in the feedstock. In this case, the theoretical maximum yield of C_{16} + C_{15} HC, derived from palmitic acid in the feedstock, was lower than the real amounts identified. This suggests these compounds did not originate solely from the palmitic acid in the feedstock, though the differences observed never exceeded +

10 mol. %. It is also consistent with the previous observation, since larger chain HC (such as C_{18} HC and C_{17} HC) can undergo HCK or hydrogenolysis to form smaller chain HC, such as C_{16} HC, C_{15} HC and CH_4.

2.2.2. Hydrodeoxygenation

The next step was to link the aqueous and organic products through stoichiometric balances. Assuming complete HDO, a 1:2 stoichiometric ratio between HC and water is expected, whereas DCO predicts a 1:1:1 ratio between HC, CO and water. From the product distribution, it was already evident that both HDO and DCO occurred, given the presence of C_{17} HC and C_{18} HC as main products. This was confirmed through the stoichiometric analysis. When complete HDO and complete DCO were considered separately solely for oleic acid, the theoretical water production in both cases exceeded the experimental value, calculated based on the outlet molar flowrate of the aqueous fraction. However, when the real molar flowrates of C_{18} + C_{16} HC (for HDO) and C_{17} + C_{15} HC (for DCO) were considered, the predicted water production was lower than the measured value in both cases. For TOS = 36 h, the gap was roughly - 5 mol. %, but for TOS = 60 h it increased to about - 20 mol. %. These discrepancies, particularly for the highest TOS, can be explained by other water-forming reactions, such as CO and CO_2 methanation. Moreover, the aqueous fraction was assumed to consist only of water, which might not be fully accurate depending on the separation efficiency. Finally, water quantification in these systems is inherently difficult due to evaporation and sampling losses.

2.2.3. Reverse water-gas shift reaction

The gaseous products were then examined in more detail. CO and CH_4 were the dominant gases, whereas CO_2 was produced in relatively small amounts and was not considered extensively at this stage. The RWGS reaction could convert CO_2 to CO, but even if all C_{17} + C_{15} HC were produced via DCO_x and the remaining CO_2 was converted, the predicted CO would still be much lower than the observed value in the case of TOS = 60 h, where the differences were approximately - 40 mol. %. For TOS = 36 h, the gap was only of roughly 2 mol. %. Therefore, the results at least for TOS = 60 h suggest RWGS was not a major pathway, though still possible most likely at lower TOS.

2.2.4. Methanation, hydrogenolysis and hydrocracking

To understand the origin of CO and CH_4 at different TOS, the analysis focused on DCO, methanation and hydrogenolysis pathways. Based on the DCO stoichiometry for both C_{17} and C_{15} products, results differed at different TOS. At TOS = 36 h the theoretical CO production was higher than the real value, while at TOS = 60 h it was lower. However, CO is also a precursor for CH_4 via methanation, which complicates the balance. The absolute theoretical maximum CH_4 was first calculated assuming complete DCO/DCO_x followed by complete CO/CO_2 methanation, providing an upper bound for CH_4 formation. This value was higher than the experimental value, as expected, since not all CO/CO_2 was converted, in both cases. To assess whether

hydrogenolysis could be a significant source of CH_4, a second limiting case was evaluated. Possible hydrogenolysis products can range from C_{17} to shorter HC. Assuming a single hydrogenolysis step, for each 17 carbon atoms, a CH_4 molecule is produced, according to stoichiometry. Summing up the carbon molar flowrates of all these HC and dividing by 17 gave a theoretical CH_4 production higher than the real value, in both cases. For TOS = 36 h with nearly + 40 mol. % (relative to the measured value) and for TOS = 60 h, where CH_4 contribution is very low, the value far exceeded the experimental one (around + 255 mol. %, relative to the measured value), suggesting that the relative contribution of CH_4 sources changes over time. As mentioned previously, for TOS = 36 h, the theoretical CO production was already higher than the experimental value, with a difference of around + 8 mol. %. However, for TOS = 60 h, there was still an unaccounted amount of CO besides from DCO. However, if instead of hydrogenolysis, which theoretically produced an amount of CH_4 far exceeding the real value, CO methanation is considered, it can totally account for the real CH_4 amount and leaves the unaccounted CO fraction to just around - 12 mol. Overall, the analysis suggests a shift in reaction pathways with TOS. Initially, hydrogenolysis contributes significantly to CH_4 formation. At higher TOS, however, the CH_4 production despite continued formation of light HC (see Fig. S7) suggests a transition towards HCK rather than hydrogenolysis.

2.2.5. Summary

In summary, considering the information gathered, the main conclusions were that C_{18} HC and C_{17} HC, once formed, undergo subsequent reactions; C_{16} HC and C_{15} HC cannot be explained solely by palmitic acid present in the feedstock, and must also originate from secondary reactions; the DCO pathway appears more selective than DCO_x; and the sources of CH_4 seem to shift with increasing TOS. These findings support the pathway analysis provided in the main document.

2.3. Product distributions

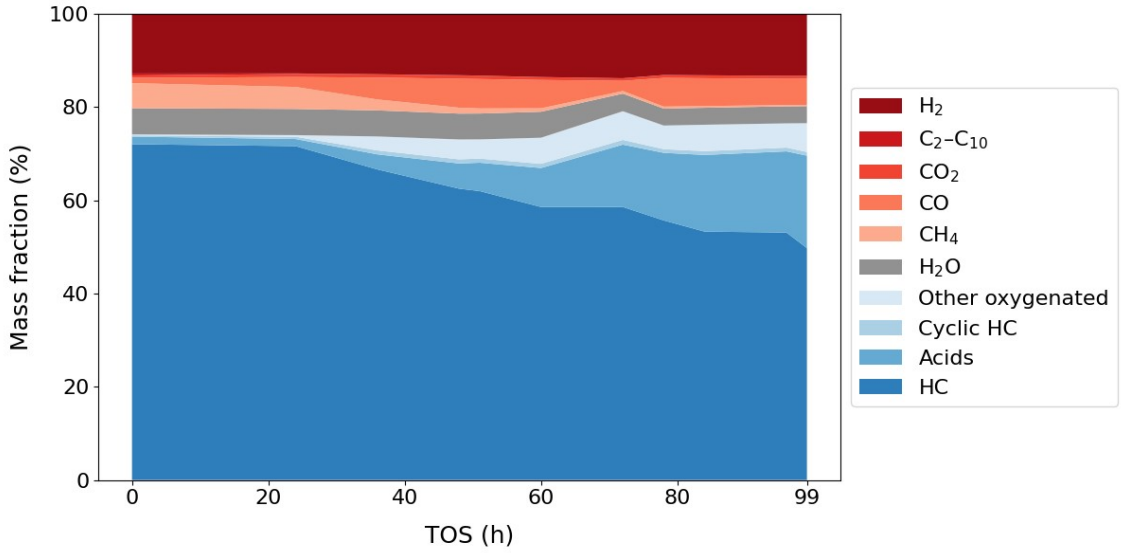

Fig. S7 Product distribution evolution during oleic acid hydroprocessing over 20Ni/HZSM-5 (P = 40 bar, T = 360 ºC, H_2/oleic acid = 1000 NmL/mL, WHSV = 9.4 h^{-1}). The blue gradient corresponds to organic products and the red gradient to gaseous products. Unreacted feedstock is included, and TOS is defined according to Section 1.3.

From Fig. S7, it is clear that the product distribution evolved over time. Initially, the main products included HC (paraffins, olefins and isomers), such as C_{17} and C_{18} HC, together with CH_4. However, with increasing TOS, the HC fraction decreased, while the production of acids, particularly stearic acid, increased. Other oxygenated products, including esters, alcohols and ethers, followed a similar trend, suggesting a progressive decline in deoxygenation efficiency. Cyclic HC, absent at the beginning of the test, appeared later but always remained below 1 wt. %. Moreover, it is possible to observe H_2 remained in excess throughout the experiment. This was confirmed through a stoichiometric estimation assuming a worst-case scenario of full conversion via HDO, the reaction consuming the largest amount of H_2 among the expected pathways and considering the feedstock composition. In this scenario, HDO consumes 4 moles of H_2 per mole of oleic acid; 5 moles of H_2 per mole of linoleic acid; and 3 moles of H_2 per mole of stearic/palmitic acid (vide Fig. 1). Thus, considering the feed flowrate, the corresponding stoichiometric H_2 requirement would be 38 mmol/h, whereas the actual H_2 inlet flowrate was 134 mmol/h. This confirms that H_2 was supplied in excess under the selected H_2/oleic acid = 1000 NmL/mL.

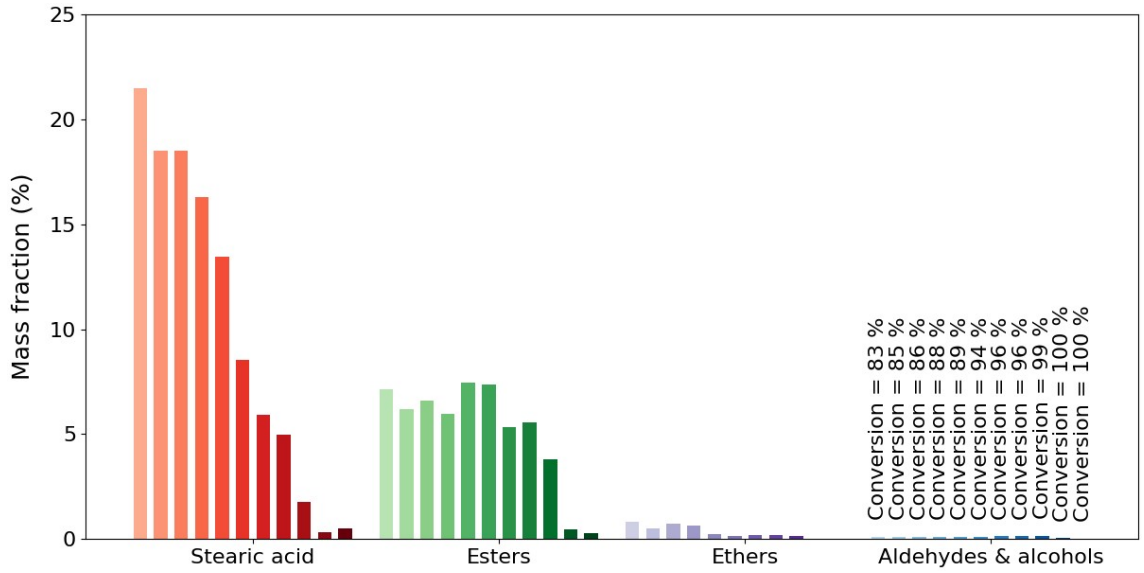

Fig. S8 Main oxygenated product distribution evolution in the organic phase during oleic acid hydroprocessing over 20Ni/HZSM-5 (P = 40 bar, T = 360 ºC, H_2/oleic acid = 1000 NmL/mL, WHSV = 9.4 h^{-1}). From left to right, each set of eleven bars represents the evolution with feedstock conversion (> 80 %).

The conversion profiles presented in Fig. 2 account for fatty acids conversion. However, a more detailed analysis revealed that linoleic acid was not detected in the organic phase, indicating it was fully converted to oleic acid through hydrogenation. Furthermore, when considering oleic acid individually, in both cases, its conversion remained relatively high (> 80 %). This means that stearic acid was the compound primarily dictating the overall conversion levels, the main acid detected in both the single-feed and simultaneous hydroprocessing experiments (vide Fig. S8 and Fig. S14a).

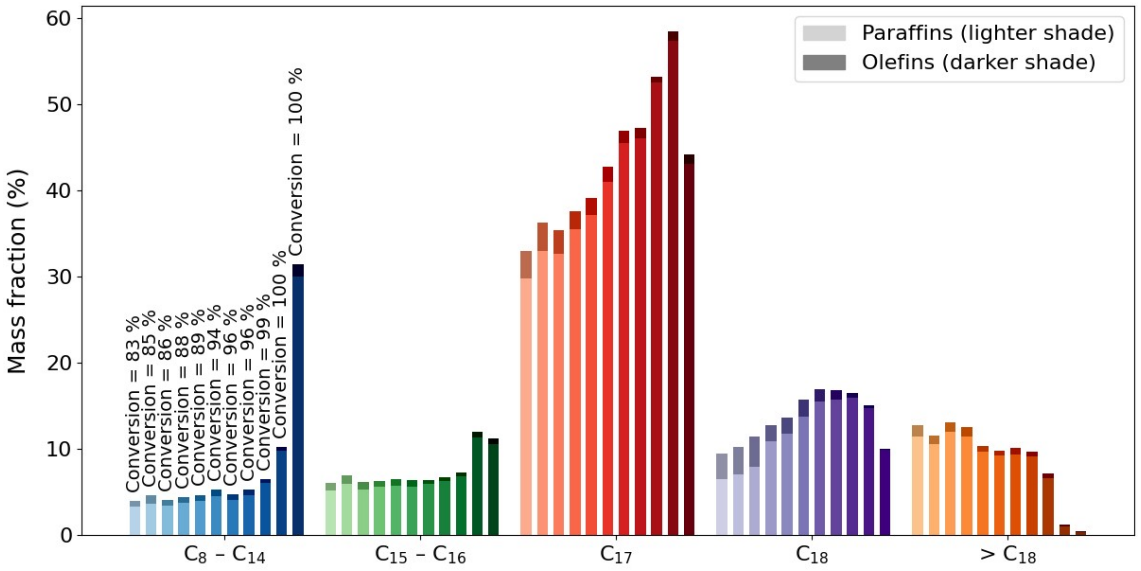

Fig. S9 Hydrocarbons evolution in the organic phase during oleic acid hydroprocessing over 20Ni/HZSM-5 (P = 40 bar, T = 360 ºC, H_2/oleic acid = 1000 NmL/mL, WHSV = 9.4 h^{-1}). From left to right, each set of eleven bars represents the evolution with feedstock conversion (> 80 %). Within each bar, the lighter shade corresponds to paraffins, whereas the darker shade corresponds to olefins.

Fig. S9 shows that the HC included both paraffins and olefins. The proposed reaction pathways (Fig. 1) include direct dehydration of oleic acid to 9-octadecene. This pathway was inferred from the selective production of this compound, which retains the original double bond position of oleic acid.

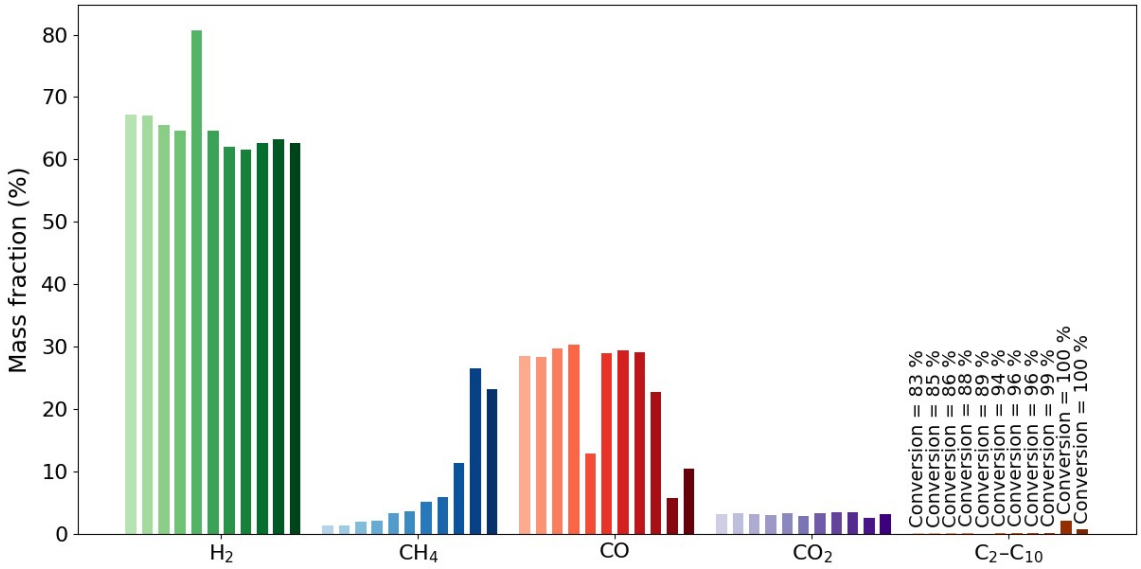

Fig. S10 Gaseous products evolution during oleic acid hydroprocessing over 20Ni/HZSM-5 (P = 40 bar, T = 360 ºC, H_2/oleic acid = 1000 NmL/mL, WHSV = 9.4 h^{-1}). From left to right, each set of eleven bars represents the evolution with feedstock conversion (> 80 %).

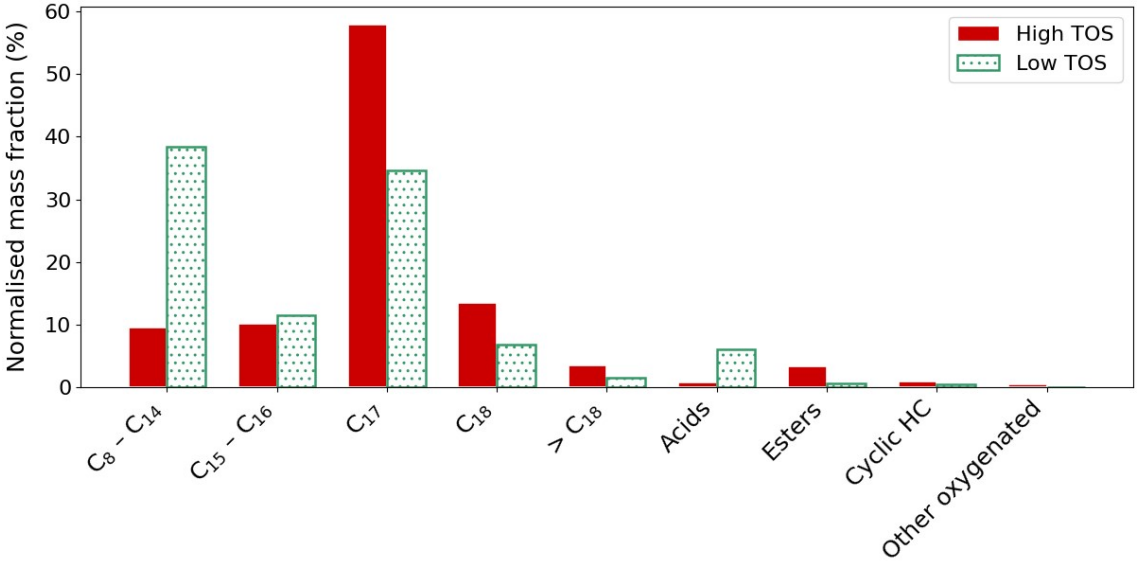

Fig. S11 Product distribution evolution in the organic phase for single-feed (oleic acid) hydroprocessing over 20Ni/HZSM-5 (excluding linoleic acid, oleic acid and stearic acid) at iso-conversion (~ 97 %). Common operating conditions: P = 40 bar, T = 340 ºC, H_2/oleic acid = 1000 NmL/mL. High TOS (~ 111 h): WHSV = 9.4 h^{-1}. Low TOS (~ 36 h): WHSV = 2.0 h^{-1}.

Fig. S11 demonstrates the deactivation effects on oleic acid hydroprocessing using different operating conditions (T = 340 ºC, P = 40 bar, H_2/oleic acid = 1000 NmL/mL, WHSV = 9.4 h^{-1} and 2.0 h^{-1}).

Fig. S9 shows some different trends over time. At the start of the experiment, light HC (C_8 - C_{14}) were abundant, but rapidly declined within 24 h and stabilised after 36 h. Considering the parallel trend for CH_4 (vide Fig. S10), this suggests initially that the light HC were mainly formed by hydrogenolysis of larger HC [18]. Over time, their fraction stabilised faster than CH_4, which may indicate that CO/CO_2 methanation also contributed to CH_4 formation early on, but decreased with TOS, consistent with the stoichiometric analysis (refer to Section 2.2) and Fig. S11. Additionally, the low CO_2 mass fraction across the experiment suggests DCO was more favourable than DCO_x.

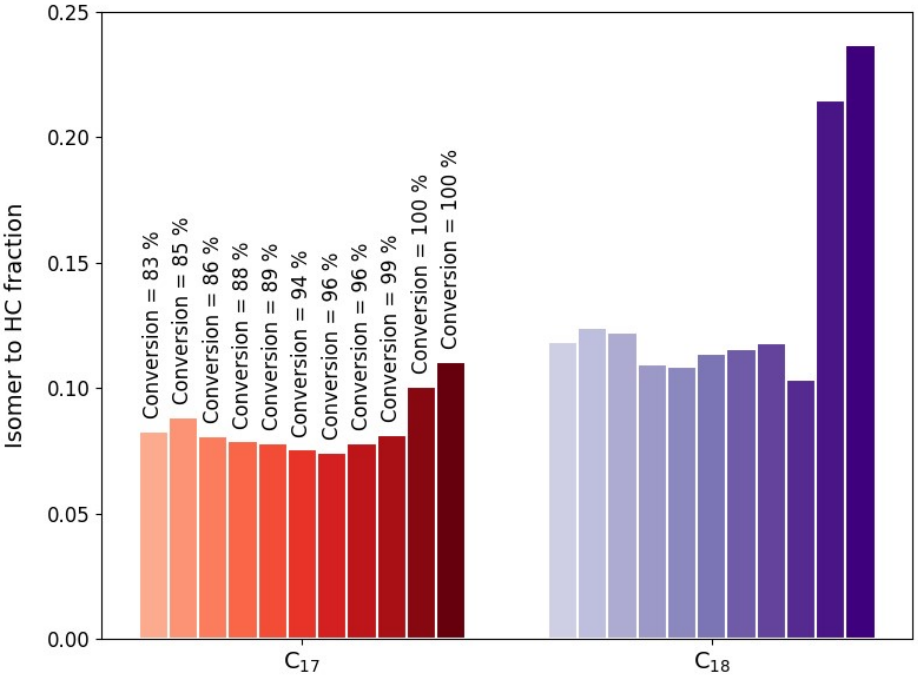

Fig. S12 Isomer to hydrocarbon ratio in the organic phase during oleic acid hydroprocessing over 20Ni/HZSM-5 (P = 40 bar, T = 360 ºC, H_2/oleic acid = 1000 NmL/mL, WHSV = 9.4 h^{-1}). From left to right, each set of eleven bars represents the evolution with feedstock conversion (> 80 %).

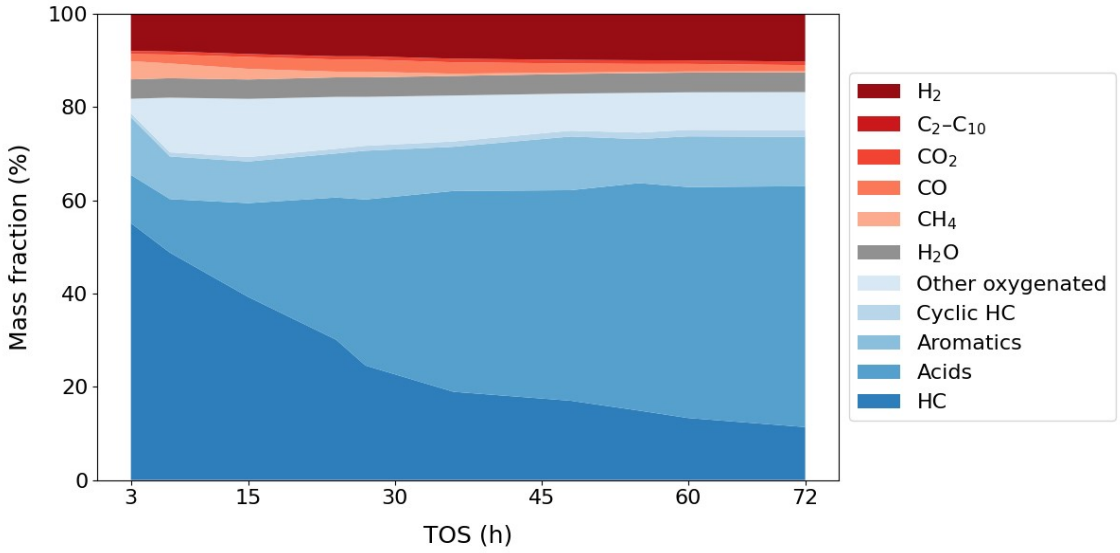

Fig. S13 Product distribution evolution during oleic acid hydroprocessing over 20Ni/HZSM-5 (P = 40 bar, T = 360 ºC, H_2/oleic acid = 1000 NmL/mL, WHSV = 9.4 h^{-1}). The blue gradient corresponds to organic products and the red gradient to gaseous products. Unreacted feedstock is included, and TOS is defined according to Section 1.3.

3. Mixture effects between oleic acid and guaiacol

From Fig. S13, it is evident that the product distribution evolved during the experiment, following a similar qualitative trend to that observed in the single-feed test (vide Fig. S7). In particular, HC, mainly C_{17} and C_{18}, dominated in the early stages but progressively decreased with time, while acids, primarily stearic acid, became increasingly prominent. The gradual replacement of HC by oxygenated products again suggests a decline in overall deoxygenation efficiency. Cyclic HC remained a minor fraction throughout (< 1.5 wt. %), but almost doubled over time. The presence of excess H_2 was also verified through a stoichiometric estimation assuming a worst-case scenario of full oleic acid conversion via HDO and complete guaiacol conversion to cyclohexane through phenol production via catechol, the pathways consuming the largest amount of H_2. In this scenario, guaiacol conversion to cyclohexane consumes 6 moles of H_2 per mole of guaiacol, while the corresponding reactions for oleic acid were presented in Fig. 1. Hence, considering the feed flowrate and composition, the corresponding stoichiometric H_2 requirement would be 74 mmol/h, whereas the actual H_2 inlet flowrate was 141 mmol/h, confirming H_2 was supplied in excess.

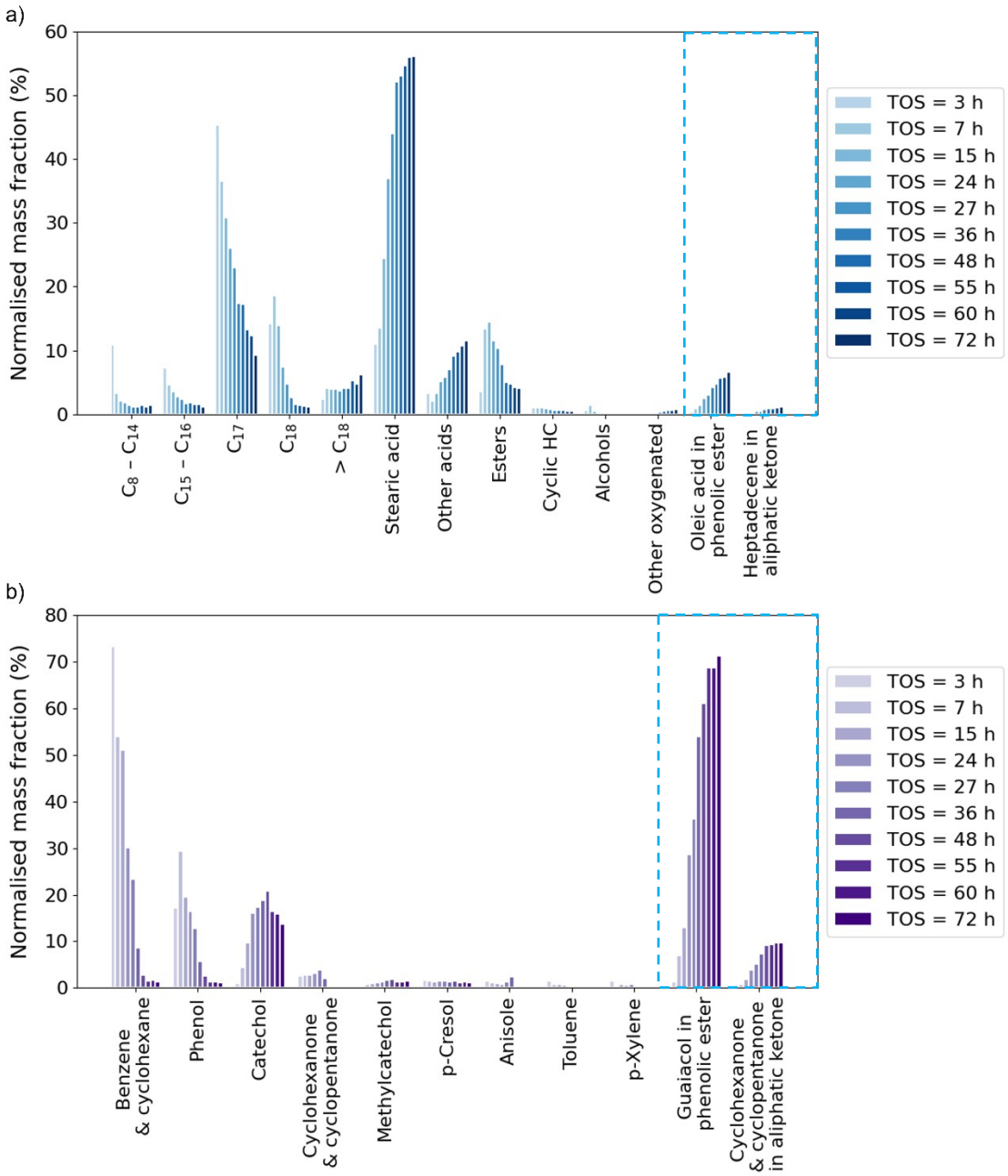

Fig. S14 Product distribution evolution in the organic phase during simultaneous hydroprocessing: a) oleic acid-derived products; b) guaiacol-derived products. The dashed area accounts for the estimated mixed-origin products.

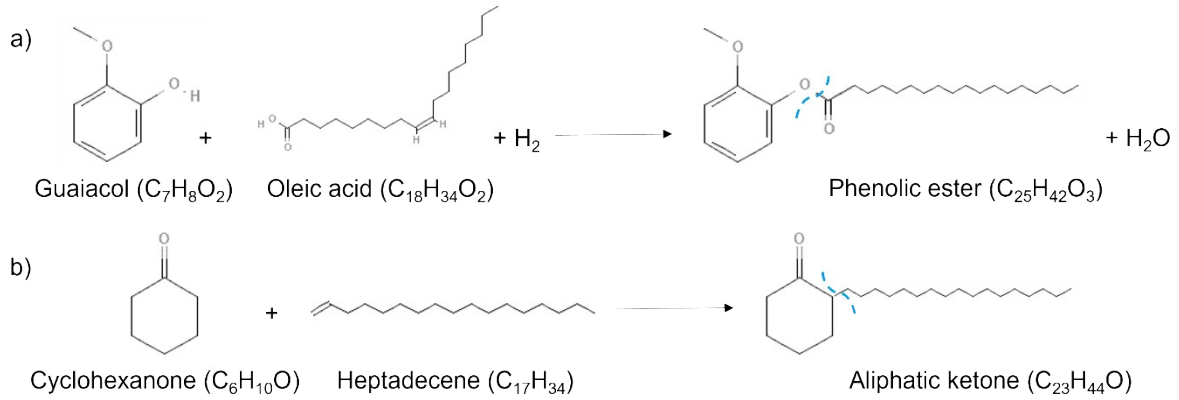

Fig. S15 Proposed reaction pathways for mixed-origin products: a) phenolic esters; b) aliphatic ketones. The dashed line separates oleic acid and guaiacol-derived structures.

The mixed-origin products, most likely, originated from both oleic acid and guaiacol. Thus, it was necessary to separate each of the feedstock's contributions to these products, based on the molecular weights of the respective structural fragments (according to Fig. S15). This ensured a reliable comparison of single-feed and simultaneous hydroprocessing conditions.

It should be noted that, for both mixed-origin families, structural rearrangements are possible and may result in different ring substitution patterns for the HC chain. The structures presented in Fig. S15 are therefore illustrative, intended to show representative pathways rather than definitive ones.

Considering Fig. 3b, when the acids incorporated into phenolic esters were accounted for, the observed discrepancies were reconciled. A similar correction applies to the C_{17} HC, where the lower apparent mass fraction in the simultaneous hydroprocessing experiment can be compensated by the heptadecene incorporated into the aliphatic ketones. Heptadecene, however, can also be hydrogenated to heptadecane, meaning there is likely competition between these two routes.

4. Additional references

[1] Song M, Zhang X, Chen Y, Zhang Q, Chen L, Liu J, et al. Hydroprocessing of lipids: An effective production process for sustainable aviation fuel. Energy 2023;283. https://doi.org/10.1016/j.energy.2023.129107.

[2] Gollakota ARK, Shu CM, Sarangi PK, Shadangi KP, Rakshit S, Kennedy JF, et al. Catalytic hydrodeoxygenation of bio-oil and model compounds - Choice of catalysts, and mechanisms. Renewable and Sustainable Energy Reviews 2023;187. https://doi.org/10.1016/j.rser.2023.113700.

[3] Žula M, Grilc M, Likozar B. Hydrocracking, hydrogenation and hydro-deoxygenation of fatty acids, esters and glycerides: Mechanisms, kinetics and transport phenomena. Chemical Engineering Journal 2022;444:136564. https://doi.org/10.1016/j.cej.2022.136564.

[4] Costa DP, Fernandes A, S.-Aguiar EF, Alves C, Ferreira P, Lopes JCB, et al. Exploring the influence of zeolite textural properties on the production of sustainable fuels through the Fischer-Tropsch process. Appl Catal A Gen 2025;692:120095. https://doi.org/10.1016/j.apcata.2024.120095.

[5] Wang R, Xia C, Peng B. Fundamental understanding and catalytic applications of hollow MFI-type zeolites. Catal Today 2022;405–406:111–24. https://doi.org/10.1016/j.cattod.2022.06.026.

[6] Verboekend D, Antoine D'Halluin M. Zeolite-y and catalyst comprising zeolite-y. WO2024194193A1, 2024.

[7] Dalena F, Dib E, Onida B, Ferrarelli G, Daturi M, Giordano G, et al. Evaluation of Zeolite Composites by IR and NMR Spectroscopy. Molecules 2024;29:4450. https://doi.org/10.3390/molecules29184450.

[8] EUROKIN. EUROKIN spreadsheet for assessment of transport limitations in gas-solid fixed beds 2012. https://www.eurokin.org/wp-content/uploads/webtool/EUROKIN_fixed-bed_html.htm (accessed May 8, 2025).

[9] Parkinson DR. Analytical Derivatization Techniques. Comprehensive Sampling and Sample Preparation, vol. 2, Elsevier; 2012, p. 559–95. https://doi.org/10.1016/B978-0-12-381373-2.00060-0.

[10] Orata F. Derivatization Reactions and Reagents for Gas Chromatography Analysis. Advanced Gas Chromatography - Progress in Agricultural, Biomedical and Industrial Applications, InTech; 2012. https://doi.org/10.5772/33098.

[11] Dietz WA. Response Factors for Gas Chromatographic Analyses. J Chromatogr Sci 1967;5:68–71.

[12] Augustine RL. Whither Goest Thou, Catalysis. Catal Letters 2016;146:2393–416. https://doi.org/10.1007/s10562-016-1865-8.

[13] Mattson B, Foster W, Greimann J, Hoette T, Le N, Mirich A, et al. Heterogeneous Catalysis: The Horiuti–Polanyi Mechanism and Alkene Hydrogenation. J Chem Educ 2013;90:613–9. https://doi.org/10.1021/ed300437k.

[14] Sun X, Chen J, Hu P. General trends in Horiuti-Polanyi mechanism vs non-Horiuti-Polanyi mechanism for water formation on transition metal surfaces. Chinese Journal of Catalysis 2020;41:294–301. https://doi.org/10.1016/S1872-2067(19)63434-0.

[15] Cousin FE, Hongkailers S, Pongpimai K, Saiyasombat C, Hinchiranan N, Samec JSM, et al. Selective Hydrogenation of Fatty Acids to Fatty Alcohols over Bifunctional Ni-Mo-

Based Catalyst Supported on Zr-SBA-15. ACS Sustain Chem Eng 2025;13:21430–44. https://doi.org/10.1021/acssuschemeng.5c07097.

[16] Liu Z, Mei J, Kong X, Li D, Zou Y, Wang C, et al. Revealing the mechanism of selective hydrogenation of oleic acid on bifunctional hierarchical catalysts. J Catal 2025;450:116274. https://doi.org/10.1016/j.jcat.2025.116274.

[17] Mannu A, Mele A. Fischer-Speier Esterification and Beyond: Recent Mechanicistic Advances. Catalysts 2024;14:931. https://doi.org/10.3390/catal14120931.

[18] Li M, Xing S, Yang L, Fu J, Lv P, Wang Z, et al. Nickel-loaded ZSM-5 catalysed hydrogenation of oleic acid: The game between acid sites and metal centres. Appl Catal A Gen 2019;587:117112. https://doi.org/10.1016/j.apcata.2019.117112.

[19] Song W, Liu Y, Baráth E, Wang LL, Zhao C, Mei D, et al. Dehydration of 1-Octadecanol over H-BEA: A Combined Experimental and Computational Study. ACS Catal 2016;6:878–89. https://doi.org/10.1021/acscatal.5b01217.

[20] Badin EJ, Pacsu E. Mechanism of Catalytic Hydrogenation and Dehydrogenation of Aldehydes and Alcohols. J Am Chem Soc 1944;66:1963–8. https://doi.org/10.1021/ja01239a053.

[21] Rahmawati Z, Santoso L, McCue A, Azua Jamari NL, Ninglasari SY, Gunawan T, et al. Selectivity of reaction pathways for green diesel production towards biojet fuel applications. RSC Adv 2023;13:13698–714. https://doi.org/10.1039/d3ra02281a.

[22] Weitkamp J. Catalytic Hydrocracking—Mechanisms and Versatility of the Process. ChemCatChem 2012;4:292–306. https://doi.org/10.1002/cctc.201100315.